A robust Au-C≡C anchoring group greatly improves the signal stability of electrochemical aptamer-based sensors for in-vivo measurements

Wanxue Zhang[1], Bandar Alsuwayni[2,3], Jiamei Liu[1], Qingqing Wu[2], Ziyin Mei[1], Songjun Hou[2], Zishuo Zhang[1], Xuewei Du[1], Suyan Yi[1], Shaoguang Li[1], Colin Lambert[2],* Hui Li[1],* Fan Xia*

[1]*State Key Laboratory of Geomicrobiology and Environmental Changes, Engineering Research Center of Nano-Geomaterials of Ministry of Education, Faculty of Materials Science and Chemistry, China University of Geosciences, Wuhan 430074, China*

[2]*Lancaster University, Faculty of Science and Technology, Lancaster University Department of Physics, Lancaster LA1 4YB, England*

[3]*University of Hail, Faculty of Science, Physics Department, Kingdom of Saudi Arabia*

Content

Materials and Reagents. 6-mercapto-1-hexanol (MCH) was purchased from Sigma-Aldrich; 6-heptyn-1-ol (HYO) was obtained from Bide Pharmatech Ltd.; 1-hexyne (HY), 2-aminohex-5-ynoic acid hydrochloride (HYAH), and tris(2-carboxyethyl)phosphine hydrochloride were purchased from Sigma; 5-hexynoic acid (HA), kanamycin sulfate, vancomycin hydrochloride, triethylamine, and cesium carbonate were obtained from Aladdin; Azure I, tetrahydrofuran, cyclopentyl ether, and anhydrous acetonitrile were purchased from Alfa Aesar; trimethylamine was obtained from TCL; 1H-perfluoro-1-octyne (PFOY) was purchased from Matrix; 5-Hexyn-1-amine hydrochloride (HPGH) was obtained from MedChemExpress; 3-chloro-1-propanethiol was purchased from Macklin; 5-bromo-1-pentyne was obtained from Zhengzhou Alpha Chemical Co., Ltd.; doxorubicin hydrochloride was purchased from Adamas-beta; fluorescein isothiocyanate-labeled bovine serum albumin (FITC-BSA) was obtained from Beijing Solarbio Science & Technology Co., Ltd.; and D-(+)-anhydrous glucose was purchased from China National Pharmaceutical Group Chemical Reagent Co., Ltd. KI and K_2CO_3 were purchased from China National Medicines Corporation Ltd. All reagents were used as received.

Microcloths (~3 inches) and 1 μm and 0.05 μm alumina powders were obtained from CH Instruments Inc. Wires for electrode fabrication—gold wire (0.2 mm diameter), tungsten wire (0.2 mm diameter), and silver wire (0.1 mm diameter)—were purchased from Wuhan Xinshen Chemical Technology Co., Ltd. Phosphate-buffered saline (PBS) and blood were obtained from Shanghai YuanYe Bio-Technology Co., Ltd. (Shanghai, China), and used as received. Teflon tubing used as an insulating material was purchased from Zeus Industrial Products, Inc.

Methylene blue and thiol-modified DNA aptamers as well as methylene blue and alkyne-modified DNA aptamers were synthesized by Shanghai Sangon Biological Engineering Technology & Services Co., Ltd. The sequence of vancomycin aptamer

used in this study is as following (DNA sequences remain the same while varying the anchoring group):

5′-HS-SH-C_6H_{12}-CGAGGGTACCGCAATAGTACTTATT GTTCGCCTATTGTGGGTCGG-MB-3′.

5′-HC≡CH-C_4H_8-CGAGGGTACCGCAATAGTACTTATTGTT CGCCTATTGTGGGTCGG -MB-3′.

The sequence of kanamycin aptamer used in this study is as following (DNA sequences remain the same while the anchoring group):

5′-HS-SH-C_6H_{12}- GGGACTTGGTTTAGTAATGAGTCCC-MB-3′.

5′- HC≡CH-C_4H_8-GGGACTTGGTTTAGTAATG AGTCCC -MB-3′.

The sequence of the doxorubicin recognition aptamer used in this study is as following (DNA sequences remain the same while the anchoring group):

5′-HS-SH-C_6H_{12}-ACCATCTGTGTAAGGGGTAAGGGGTGGT-MB-3′.

5′- HC≡CH-C_4H_8-ACCATCTGTGTAAGGGGTAAGGGGTGGT -MB-3′.

Synthesis of MB-C≡CH. We followed a synthetic procedure similar to that described in a previous report, with slight modifications[1]. Under a nitrogen atmosphere, Azure I (0.369 g, 1.2 mmol) and 5-bromo-1-pentyne (150 μL, 1.4 mmol) were sequentially added to a solution of Cs_2CO_3(0.78 g, 2.4 mmol) in N, N-dimethylformamide (DMF, 3 mL). After vigorous stirring and a reaction at 50°C for 8 h, the product was purified by silica gel column chromatography and obtain the product (yield: 25.6%).

Synthesis of MB-SH. We synthesized this compound by following a similar protocol in a previous report[2]. Under a nitrogen atmosphere, Azure I (0.367 g, 1.2 mmol) and 3-chloro-1-propanethiol (137 μL, 1.4 mmol) were sequentially added to a mixture of K_2CO_3 (0.166 g, 1.2 mmol) and KI (0.199 g, 1.2 mmol) in N, N-dimethylformamide (DMF, 3 mL). After vigorous stirring and a reaction at 80°C for 5 h, the product was purified by silica gel column chromatography (yield: 1.6%).

Synthesis of HPC. The compound was synthesized following a procedure similar to that previously reported[3]. 5-Hexyn-1-ol (0.975 g, 10 mmol) and triethylamine (1.385 mL, 10 mmol) were dissolved in tetrahydrofuran (THF, 10 mL) and stirred at room temperature for 3 minutes. The solution was then cooled to -20°C to serve as the reaction mixture. 2-Chloro-2-oxo-1,3,2-dioxaphospholane (COP, 1.425 g, 10 mmol) was dissolved in THF (5 mL) and slowly added dropwise to the reaction mixture over the course of 1 hour, maintaining the temperature at approximately -20°C. The resulting

white precipitate was filtered off, and the filtrate was concentrated using a rotary evaporator and dried to afford the intermediate product. The intermediate was dissolved in anhydrous acetonitrile (7.5 mL), cooled to -20°C, and quickly mixed with trimethylamine (5.375 mL, 10.75 mmol). The reaction vessel was then sealed and heated at 60°C for 24 hours, followed by storage at -10°C for 2 hours. The resulting precipitate was collected by filtration, washed with cold acetonitrile, and dried under reduced pressure.

Electrode Cleaning. First, we performed electrochemical cleaning of the electrode using a three-electrode setup in 0.5 M NaOH solution, cycling the voltage between 0 and -1.5 V (all potentials referenced to Ag/AgCl) at a scan rate of 0.1 V s^{-1} for 10 cycles. The working electrode was then thoroughly rinsed with deionized water and transferred to 0.5 M H_2SO_4, where a chronoamperometric procedure was applied with $E_{initial}$ = 0 V, E_{high} = 2.0 V vs Ag/AgCl for 500 cycles, each pulse lasting 0.02 s. Finally, the working electrode was transferred to 0.05 M H_2SO_4, where cyclic voltammetry was performed between 0 and 1.65 V at a scan rate of 0.1 V s^{-1} to integrate the area under the oxidation and reduction peak curves, which was then divided by 422 μC cm^{-2} to determine the electroactive area of each gold electrode.

Fabrication protocols of Au-C≡CH-based EAB Sensors. First, a 0.5 μM DNA solution was prepared, diluted with 100 μM alkyne-modified DNA in 1× PBS (pH 7.5) buffer. Then, under an argon atmosphere, the cleaned electrode was incubated in the solution at 60°C for 22 h. The electrode was rinsed with deionized water and then incubated in a 1 mM HYA ethanol solution at 60°C for 20 h.

Fabrication protocols of Au-SH-based EAB Sensors. First, a 0.5 μM DNA solution was prepared, with 100 μM thiolated DNA incubated with 20 mM TCEP (1:1) for 1 hour, followed by dilution with 1× PBS (pH 7.5). The electrode was then immersed in the DNA solution at room temperature for 2 hours, rinsed with deionized water, and incubated overnight in a 1 mM MCH solution at 4°C.

The packing density of DNA on gold electrode surfaces. Based on the cyclic voltammograms obtained at a scan rate of 0.1 V/s and using Equation (1)

$$I_P = \frac{n^2 F^2 A \Gamma_{MB}}{4RT} v \quad (1)$$

Where n is the numbers of electrons of redox reporter employed (n = 2 for MB), A is the electrode surface area, v is the scanning speed, F is Faraday's constant at a value of 96485 C/mol, R is gas constant at 8.314 J/(mol • K), and T is the standardized

temperature of 298.15K. Using this equation, the probe density Γ_{MB} can be derived.

The DNA grafting density was determined to be 0.20 pmol/cm² for the alkyne-anchored EAB sensor, and 2.3 pmol/cm² for the thiol-anchored EAB sensor. Multiplying these densities by Avogadro's constant (N_A) yields the corresponding areal number densities of molecules: approximately 1.20×10^{11} molecules/cm² for the alkyne-anchored sensor and 1.38×10^{12} molecules/cm² for the thiol-anchored sensor.

Immobilization of Seven Different Terminal Group Molecules on Electrode Surfaces via Au–C≡CH. HY, HYAH, PFOY, and HPC were each prepared as 1 mM self-assembled monolayers (SAMs) solutions in ethanol. HA and HPGH were prepared as SAMs solutions in PBS and DMSO, respectively. The electrodes were incubated in these solutions under an argon atmosphere at 60°C for 20 hours.

Immobilization of MB-C≡CH and MB-SH on Electrode Surfaces. A 1 mM solution of MB-C≡CH was prepared and diluted in PBS buffer (1×, pH 7.5). The electrodes were incubated in this solution under an argon atmosphere at 60°C for 20 hours. A 1 mM solution of MB-SH was prepared and reduced with TCEP, followed by incubation at room temperature for 2 hours.

Gold Microelectrode Fabrication. Gold wire (1.5 cm, diameter 0.2 mm) and tungsten wire (8 cm, diameter 0.2 mm) were cold-welded using a conductive silver epoxy adhesive. A heat-shrinkable PTFE tube was used to insulate the tungsten wire, leaving the gold wire exposed for DNA modification and the other end (tungsten wire) for connection to a potentiostat. The gold portion of the electrodes was then electrochemically roughened to increase the surface area.

Contact Angle Measurement. The microelectrodes were physically polished and cleaned using a standard cleaning protocol. After SAM incubation, 1 μL of deionized water was dropped onto the electrode surface for contact angle measurement. In complex system experiments, following SAM formation, the electrodes were immersed in whole blood at room temperature for 1 hour. The reported contact angle values represent the average of at least three different points on three independent samples.

Preparation of implantable Microelectrodes. The gold wire (7 cm, diameter 0.2 mm) and the silver wire (6 cm, diameter 0.1 mm) were insulated with heat-shrinkable polytetrafluoroethylene tubes. The gold wire is exposed for DNA modification, following the standard sensor fablication protocol. Subsequently, the gold component of these electrodes was electrochemically roughened to increase the surface area.

Contact Angle Measurement. The electrode was physically polished and cleaned

using a standard cleaning procedure. Under an argon atmosphere, the electrode was soaked in a 1 mM terminal alkyne molecule ethanol solution and incubated at 60°C for 20 h, followed by overnight incubation with the thiol molecule MCH (1 mM) at 4°C to form a uniform SAM on the electrode surface. The contact angle was measured using 1 μL of water. In the complex system experiment, after the SAMs were prepared, the electrode was soaked in whole blood solution at room temperature for 1 h. The reported contact angle values represent the average of at least three different points on three different samples.

Electrochemical Measurements. Electrochemical measurements were conducted at room temperature using a multi-channel CHI-1040C potentiostat (CH Instruments, Austin, TX) and a standard three-electrode cell, which included a platinum counter electrode and an Ag/AgCl reference electrode. Square wave voltammetry (SWV) was performed with a potential window of -0.1 to -0.45 V, a potential step of 0.001 V, and an amplitude of 0.05 V. The sensors were interrogated using a series of square wave frequencies (2 Hz-1000 Hz) in at least three independent matrices. we conducted the titration experiments at various frequencies, achieving an optimal frequency for each SAM in order to summarize and compare their performance. The selection criterion of optimal frequency was based on the baseline stability. Specifically, the optimal frequency for HY is 30 Hz due to the baseline at lower concentrations is flat and with a good transition upon the high concentration of target molecules. Similarly, the optimal frequency for HYAH was selected as 60 Hz, HA as 120Hz, PFOY as 30Hz, HPGH as 120 Hz, HPC as 30 Hz. Electron transfer kinetics were evaluated using cyclic voltammetry (CV) at scan rates ranging from 0.1 V s^{-1} to 10 V s^{-1}, also interrogated in at least three separate matrices.

In electrochemical data processing, the normalization equation is expressed as (2)

$$Relative\ signal = \frac{i}{i_0} \times 100\% \quad (2)$$

Electrochemical impedance spectroscopy (EIS) was performed in a solution containing 5 mM ferri/ferrocyanide in 0.1 M NaCl over a broad frequency range from 100 kHz to 0.1 Hz. Based on the impedance data, the charge transfer resistance (R_{ct}) was determined by fitting with an equivalent circuit model:

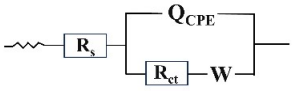

The surface coverage (θ) of the Au monolayer was then calculated using Equation

(3)[4].

$$\theta = 1 - \frac{R_{ct}^{0}}{R_{ct}} \quad (3)$$

where R_{ct}^{0} is the charge transfer resistance of bare Au electrode and R_{ct} is the charge transfer resistance of the corresponding SAM-modified electrodes.

X-ray Photoelectron Spectroscopy (XPS) Measurement. Using a monochromatic Al Kα X-ray source with an energy of 1486.6 eV, we conducted the tests. After the measurements, data analysis was performed using Avantage software, setting the binding energy (BE) of the Au $4f_{7/2}$ peak to 84.0 eV as the BE scale for the gold monolayer.

Specific Procedure for Testing VAN-C≡CH and VAN-SH. Electrodes were prepared for both VAN-C≡CH (with both DNA and SAMs anchored via alkyne groups) and VAN-SH (with both DNA and SAMs anchored via thiol groups). Four sets of each type of electrode were prepared for XPS analysis. (1) assembled but not subjected to any electrochemical scanning or contamination (immersed in blood); (2) subjected to continuous electrochemical scanning for 2 h in a whole blood system; (3) subjected to continuous electrochemical scanning for 4 h; (4) subjected to continuous electrochemical scanning for 8 h. Additionally, electrodes that were immersed in blood for 2, 4, and 8 h without electrochemical scanning were collected to account for residual contamination on the electrodes affecting the elemental content changes.

The percentage content of C (or S) elements on the gold electrode surface was calculated using the following formula (4):

$$C(or\ S) = \left(\frac{X_n}{X_0} - \frac{X'_n - X'_0}{X'_0}\right) \times 100\% \quad (4)$$

where C (or S) is the percentage change in carbon (or sulfur) element content, X_n is the percentage content of C (or S) on the electrode surface after n hours of electrochemical scanning (n=0, 2, 4, 8), and X'_n is the percentage content of C (or S) on the electrode surface after n hours of immersion in blood (n=0, 2, 4, 8).

The sampling procedure for MB-C≡CH and MB-SH for XPS measurements. Four sets of each type of electrode were prepared for XPS analysis. (1) Fully assembled but without any electrochemical scanning; (2) Subjected to continuous electrochemical scanning in buffer for 24 hours; (3) Subjected to continuous electrochemical scanning in buffer for 48 hours; (4) Subjected to continuous electrochemical scanning in buffer for 72 hours.

The percentage of carbon (or sulfur) element on the gold electrode surface was calculated using the following formula (5):

$$C(or\ S) = \frac{X_n}{X_0} \times 100\% \quad (5)$$

where X_n represents the percentage of carbon (or sulfur) on the electrode surface after n hours of electrochemical scanning in buffer (n =0, 24, 48, 72).

Confocal Microscopy Study. The antifouling performance of SAMs with different structural characteristics was evaluated using confocal microscopy. Freshly cleaned gold wires (coated with different monolayers) were immersed in a fluorescein isothiocyanate (FITC)-labeled BSA solution (0.5 mg/mL) for 20 seconds. After removal, the portion of the gold wire corresponding to the electrode was used for confocal imaging. The emission spectrum of the adsorbed protein (668 nm) was recorded using a Zeiss LSM 880 confocal microscope, and ImageJ software was used to analyze the ratio of the green fluorescent (protein-covered) area to the total surface area. For MB-C≡CH and MB-SH, confocal measurements were performed based on their inherent blue fluorescence.

Theoretical Methods. In the process of simulating face-centered cubic gold, the optimized lattice constant is 4.17 Å, and a 12×12×12 k-point mesh is adopted for accurate sampling of the Brillouin zone. The resulting lattice parameter aligns well with the experimental value of 4.08 Å[5, 6]. Gold is known to predominantly expose its (111) facet, which is the most stable due to its densely packed atomic arrangement[5]. Construction of the slab model was based on the approach proposed by Ceder[7] and implemented through the VESTA software suite[8], which offers a reliable platform for constructing and visualizing atomic structures. A (3×3) four-layer Au (111) surface was modelled, with lateral dimensions of 8.85 Å×8.85 Å. To prevent artificial interactions along the z-direction, a vacuum region of 20 Å was introduced. During geometry optimization, the top three layers were allowed to relax, whereas the bottom layer was fixed to emulate bulk conditions. A kinetic energy cut-off of 500 eV was employed for all relaxation processes, and a 4×4×1 k-point mesh was used for Brillouin zone sampling. Structural and energetic optimizations were carried out using the Generalised Gradient Approximation (GGA) with the Perdew-Burke-Ernzerhof (PBE) functional[9]. Long-range dispersion interactions were included using the Becke–Johnson damping scheme[10] within a spin-polarized DFT framework. Convergence thresholds were set at 10^{-4} eV for the electronic self-consistent field and 0.02 eV/Å for

ionic forces. Bader charge analysis was performed, as implemented by the Henkelman group[11-14].

The adsorption energy (E_{ads}) for systems A and B is defined as follows:

$$E_{ads} = E_{AB} - E_A - E_B \quad (6)$$

Where E_{AB} is the total energy of the complex system, E_A represents the total energy of optimized system A, and E_B represents the total energy of optimized system B. From the definition of adsorption energy, a negative value represents a stable adsorption mechanism.

Furthermore, charge density difference (CDD) is a widely analyzed in electronic structure analysis, enabling the investigation of charge redistribution within molecules, clusters, and solid-state materials. It is particularly effective for examining the nature of interactions between molecular species and solid surfaces. The CDD is represented as follows

$$\Delta\rho = p_{AB} - p_A - p_B \quad (7)$$

Where $\Delta\rho$ is charge density difference, p_{AB} is the charge density of the complex system, p_A represents charge density of system A without further optimization, and $p_B$represents charge density of system B without further optimization.

In Vivo Experiments. The in vivo study was conducted in accordance with the Animal Care and Institutional Ethical Guidance in China. The experiment was authorized by the Animal Research Ethics Committee of Wuhan Cloud Clone Technology Co., Ltd. (certicate number: IACU24-1359).

. Rats were anesthetized in an induction chamber with 5% isoflurane. Upon full anesthesia, the oxygen concentrator was turned on, and anesthesia was maintained with 2–3% isoflurane/oxygen via a breathing mask throughout the experiment. A 22G catheter was surgically inserted into the right jugular vein of the rat for insertion of the prepared sensor, secured in place with a hemostatic clip. Simultaneously, a 24G indwelling needle was inserted into the left vein for the administration of vancomycin (or doxorubicin) and sodium heparin. After drug infusion, the animals were euthanized by overdose anesthesia.

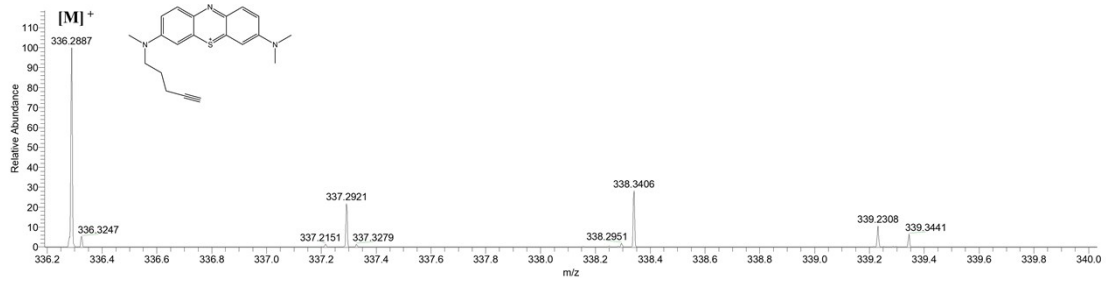

Figure S1. ESI mass spectrum of 3-(dimethylamino)-7-(methyl(pent-4-yn-1-yl) amino) phenothiazine-5-ium (Alkyne based analog compounds). The mass of Alkyne based analog compounds calculated: 336.1529 Da; observed: 336.2887 Da $[M]^+$.

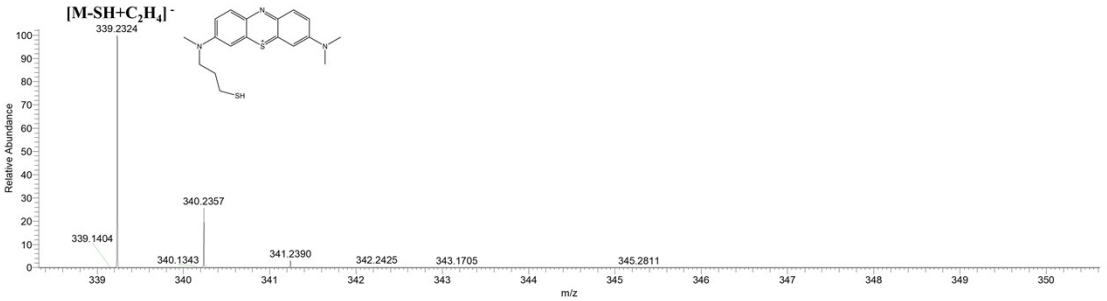

Figure S2. ESI mass spectrum of 3-(dimethylamino)-7-(3-mercaptopropyl)(methyl) amino) phenothiazin-5-ium (mercapto based analog compounds). The mass of mercapto based analog compounds calculated: 339.1764 Da; observed: 339.2324 Da $[M\text{-}SH+C_2H_4]^-$.

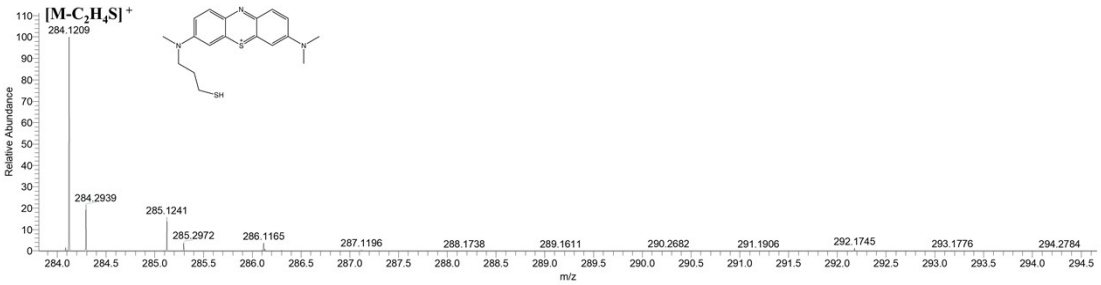

Figure S3. ESI mass spectrum of 3-(dimethylamino)-7-(3-mercaptopropyl)(methyl) amino) phenothiazin-5-ium (mercapto based analog compounds). The mass of mercapto based analog compounds calculated: 284.1216 Da; observed: 284.1209 Da $[M\text{-}C_2H_4S]^+$.

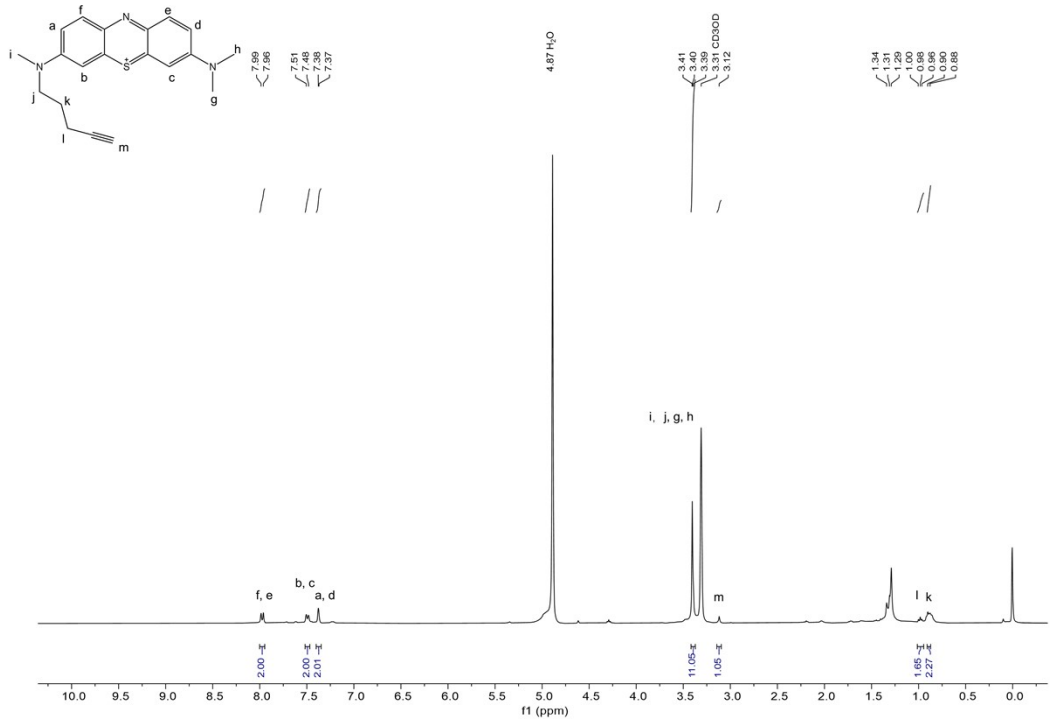

Figure S4. 1H-NMR spectrum (400 MHz, in CD_3OD). 7.96-7.99 (d, 2H), 7.48-7.51 (d, 2H), 7.38 (s, 2H), 3.39-3.41 (s, 11H), 3.12 (s, 1H), 0.96-1.00 (t, 2H), 0.88-0.90 (m, 2H).

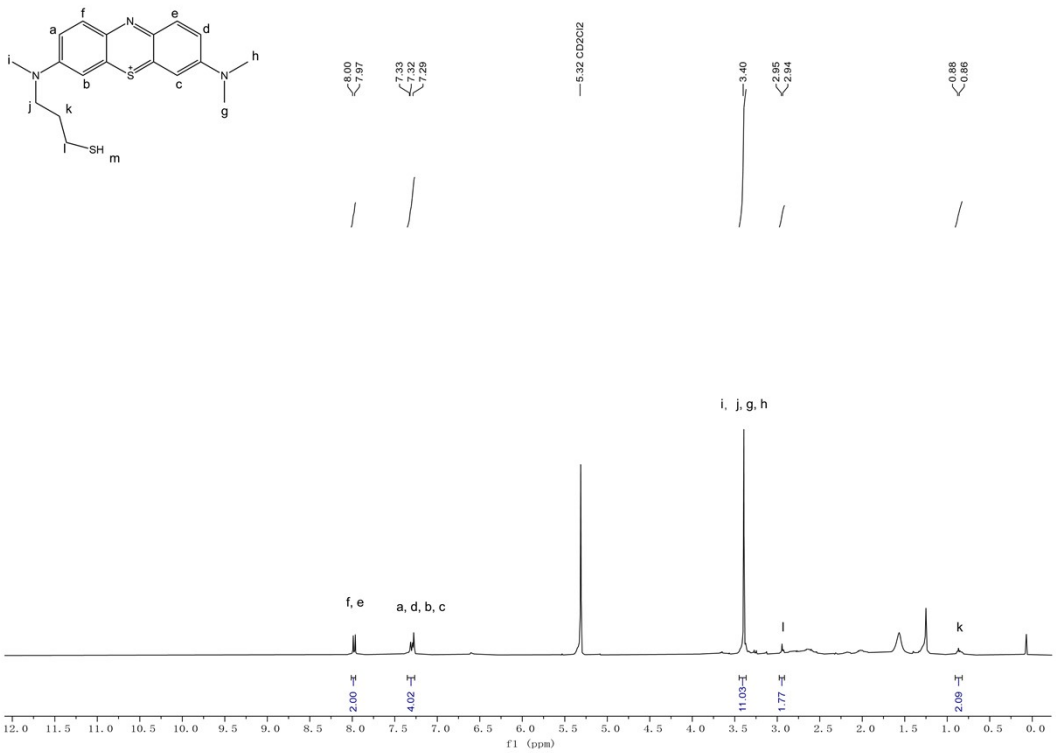

Figure S5. 1H-NMR spectrum (400 MHz, in CD_2Cl_2). 7.97-8.00 (d, 2H), 7.29-7.33 (m, 4H), 3.40 (s, 11H), 2.94-2.95 (t, 2H), 0.86-0.88 (m, 2H).

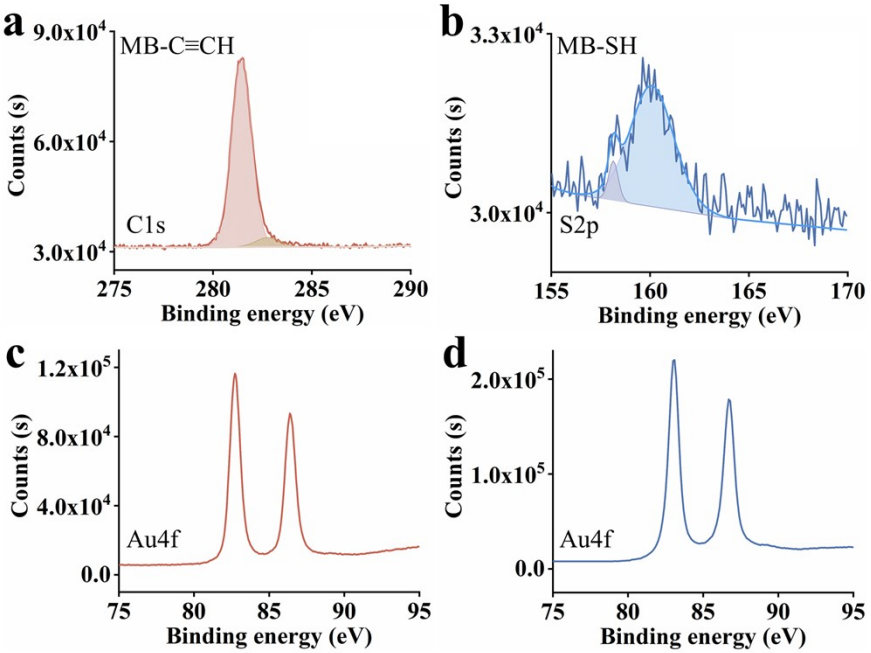

Figure S6. X-ray photoelectron spectra: (a) C1s and (c) Au4f of MB-C≡CH, (b) S2p and (d) Au4f of MB-SH.

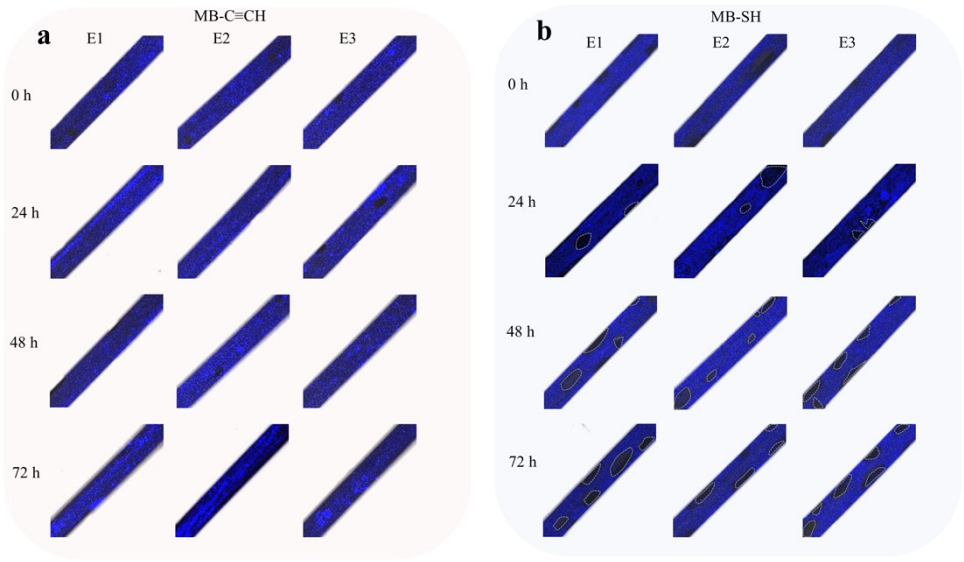

Figure S7. Confocal microscopy image: (a) MB-C≡CH-based model "EAB" sensor, (b) MB-SH-based model "EAB" sensor.

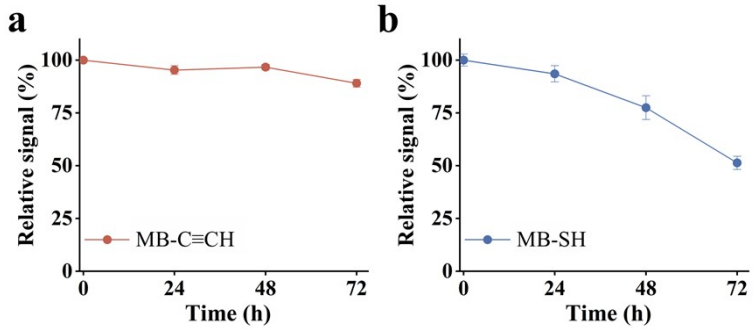

Figure S8. Temporal Changes in Surface Coverage Measured with (a) the MB-C≡CH-Based Model "EAB" Sensor, (b) MB-SH-based model "EAB" sensor.

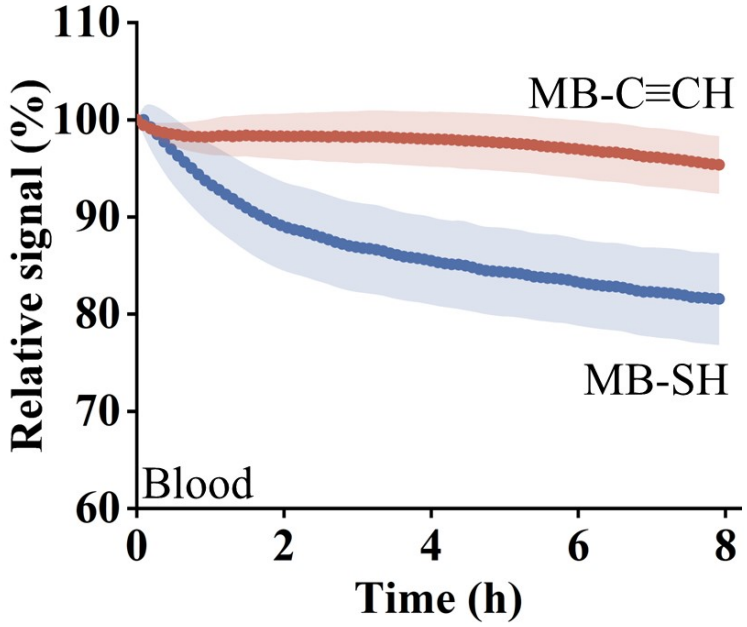

Figure S9. Signal stability of EAB sensors in blood.

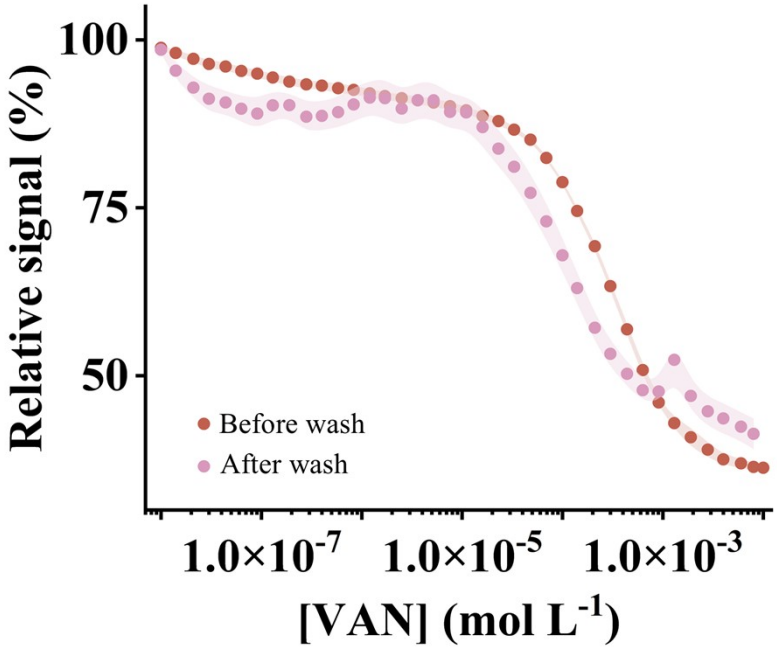

Figure S10. We achieved a reproducible titration data for VAN-C≡CH sensor prior to and after urea wash.

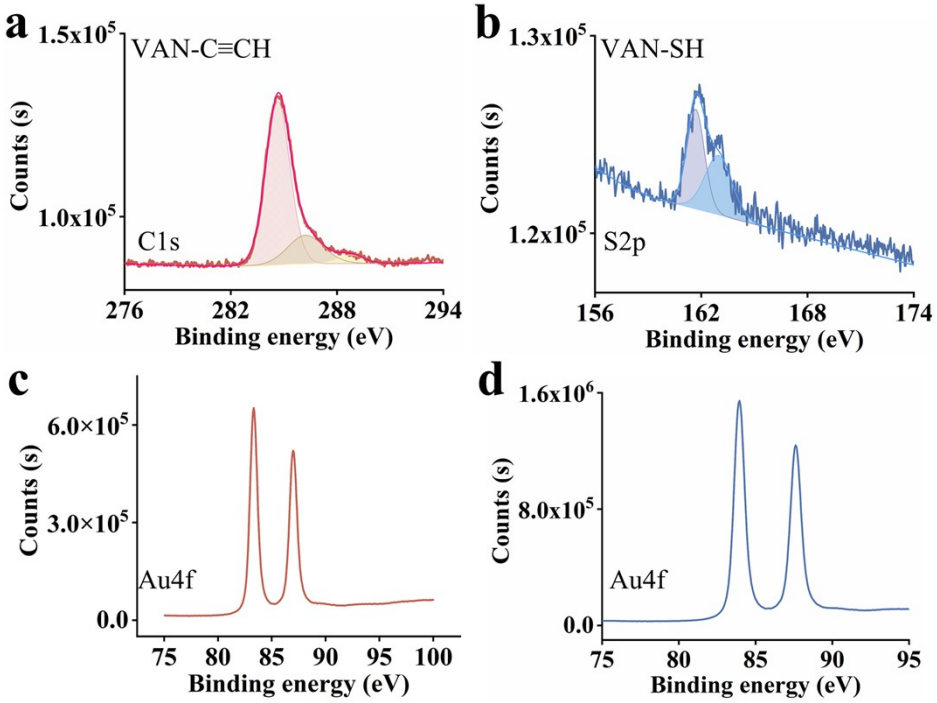

Figure S11. X-ray photoelectron spectra: (a) C1s and (c) Au4f of MB-C≡CH, (b) S2p and (d) Au4f of MB-SH.

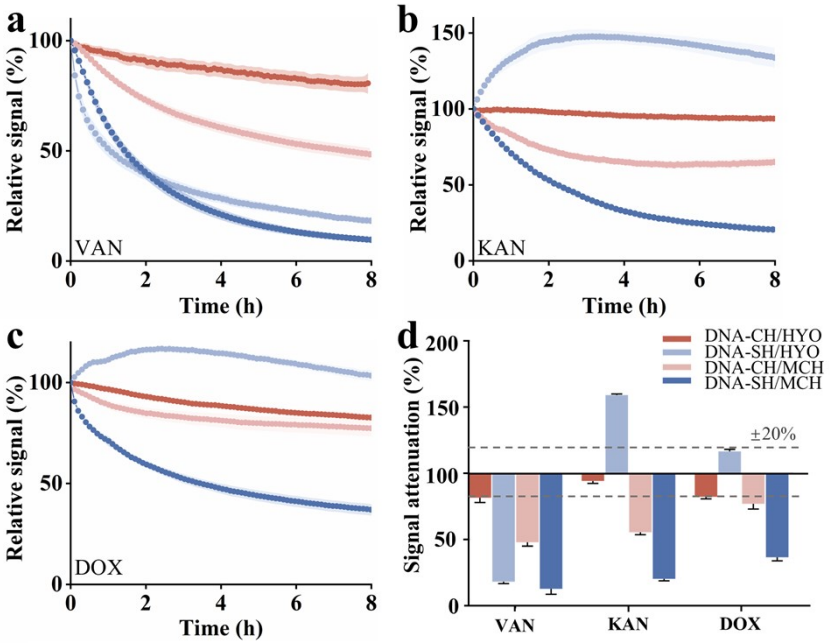

Figure S12. Stability tests in blood were conducted for aptamers and monolayers assembled using different anchoring strategies, including DNA-C≡CH/HYO, DNA-SH/HYO, DNA-C≡CH/MCH, and DNA-SH/MCH.

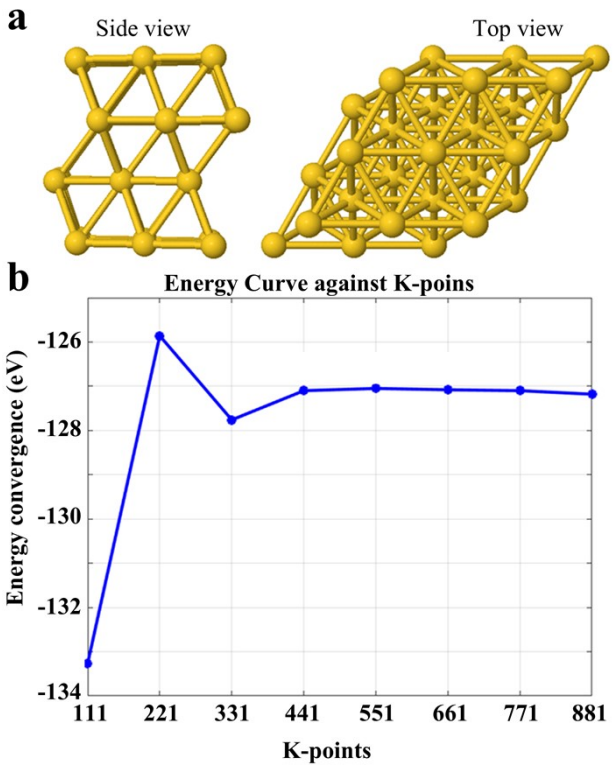

Figure S13. Geometrical configurations of gold (111) slabs and energy convergence vs K-points.

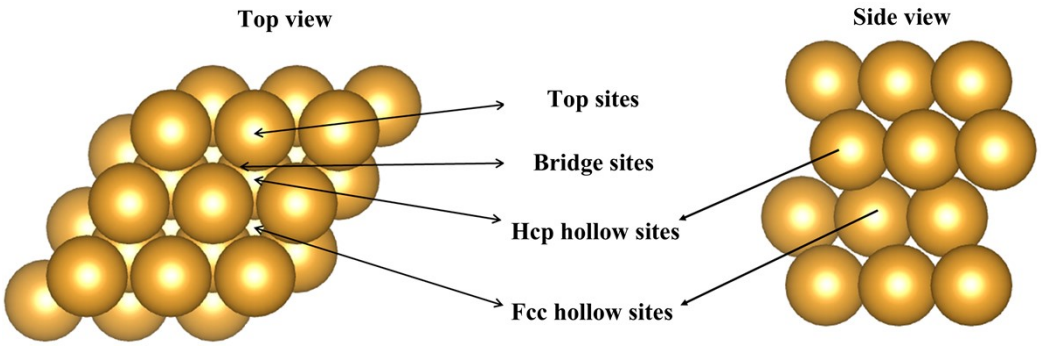

Figure S14. Four-layer Au (111) models. The four high-symmetry adsorption sites (top site, fcc- hollow site, hcp hollow site and bridge site) were denoted by arrows.

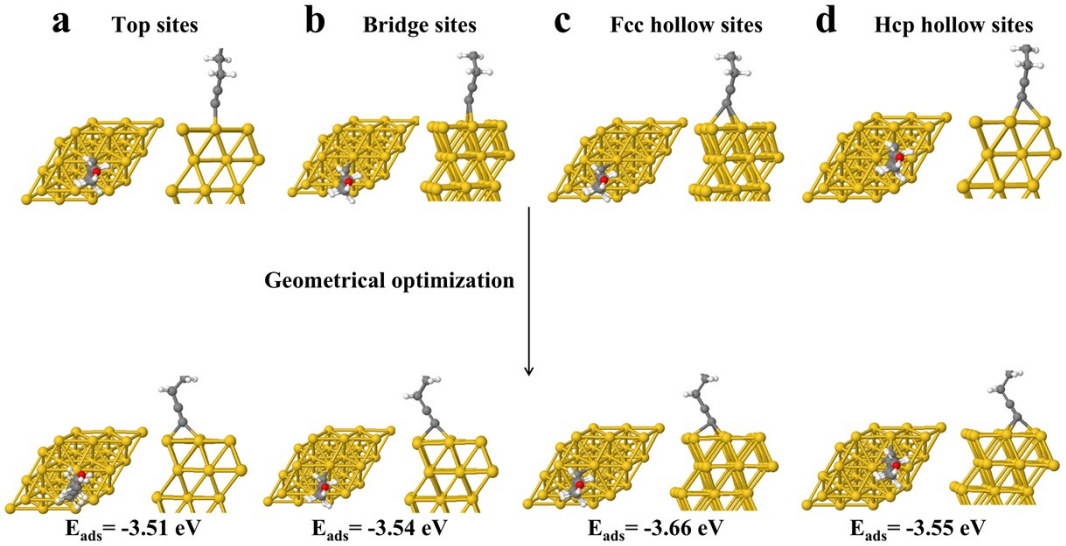

Figure S15. Optimised structures of HYA adsorbed on Au (111). The most stable structure is the one with the highest absorption energy.

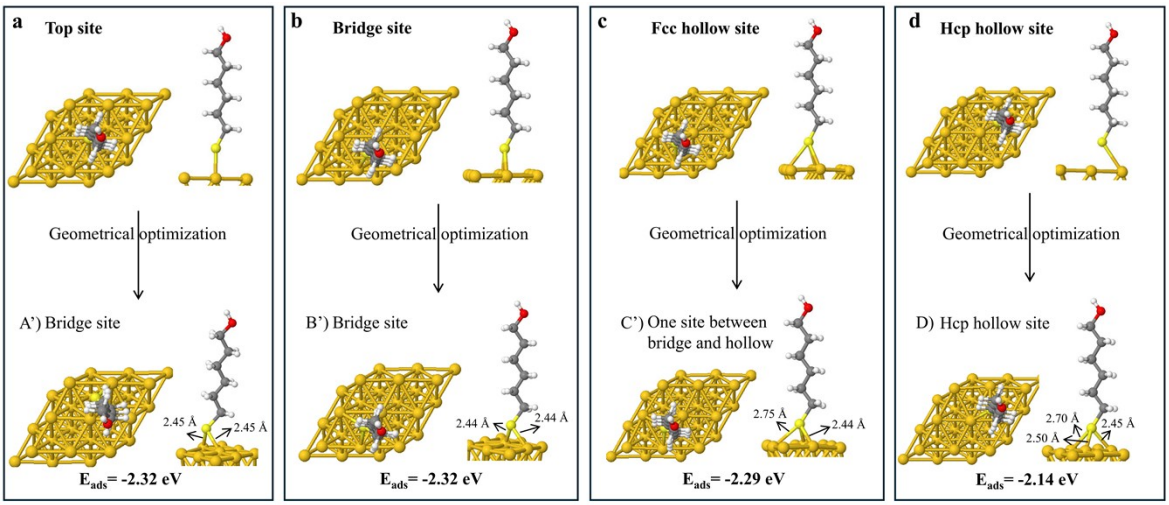

Figure S16. Optimised structures of MCH adsorbed on Au (111). The most stable structure is the one with the highest absorption energy.

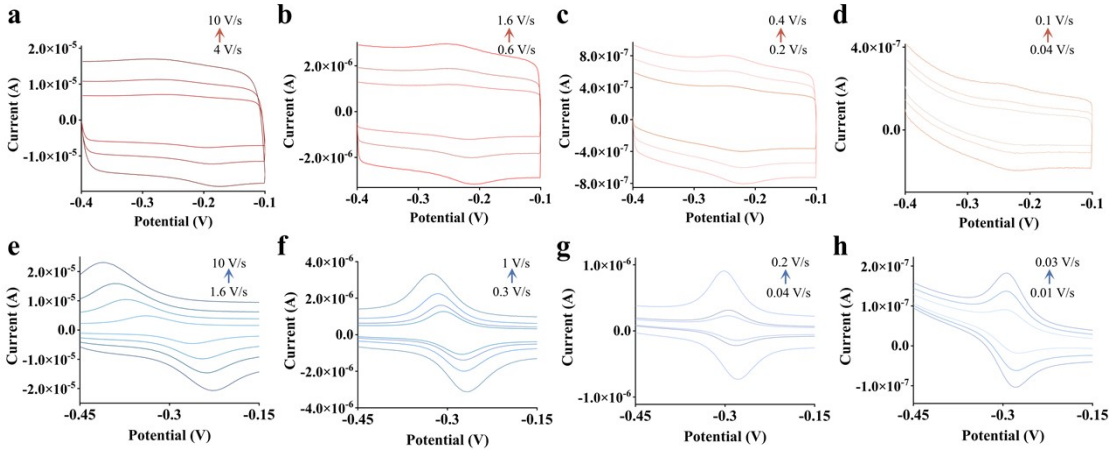

Figure S17. (a-d) VAN-C≡CH electrodes in PBS buffer at scan rates ranging from 0.04 to 10 V/s (from inner to outer curves), (e-h) VAN-SH electrodes in PBS buffer at scan rates ranging from 0.01 to 10 V/s (from inner to outer curves).

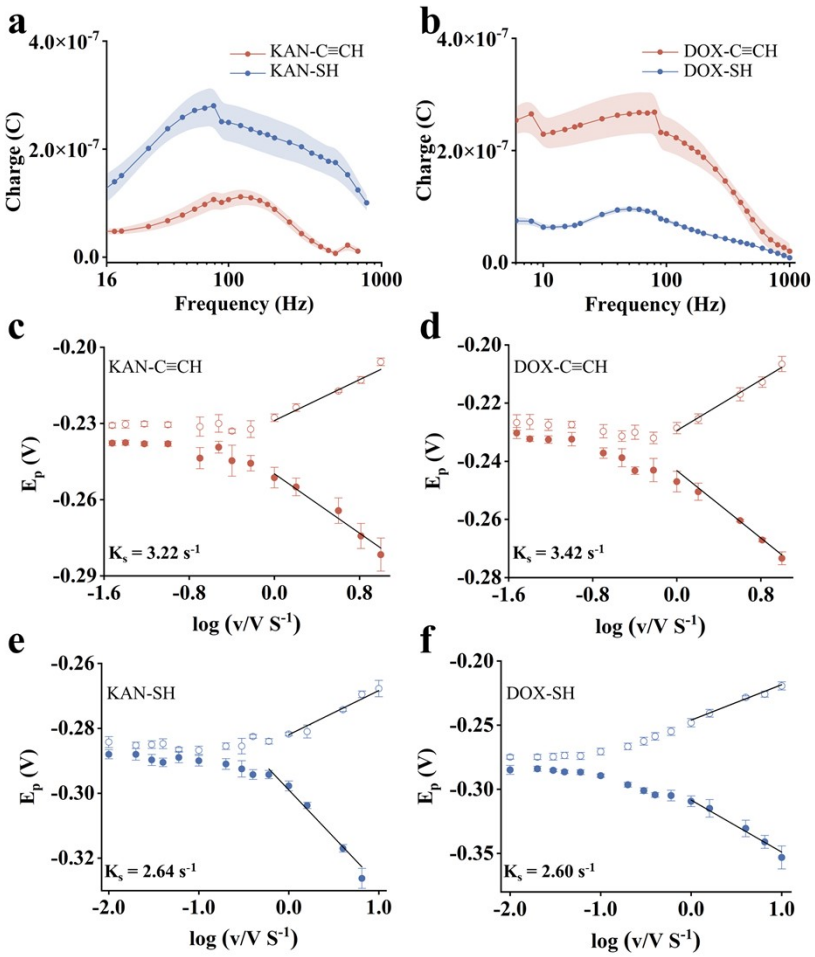

Figure S18. (a) The charge transfer function of the kanamycin-detecting EAB sensors in PBS as a function of frequency, (b) Charge transfer function of the doxorubicin-detecting EAB sensors in PBS as a function of frequency, (c) (d) Relationship between the peak potential and the logarithm of scan rate for the kanamycin-detecting EAB sensors measured by cyclic voltammetry in PBS, (e) (f) Relationship between the peak potential and the logarithm of scan rate for the kanamycin-detecting EAB sensors measured by cyclic voltammetry in PBS.

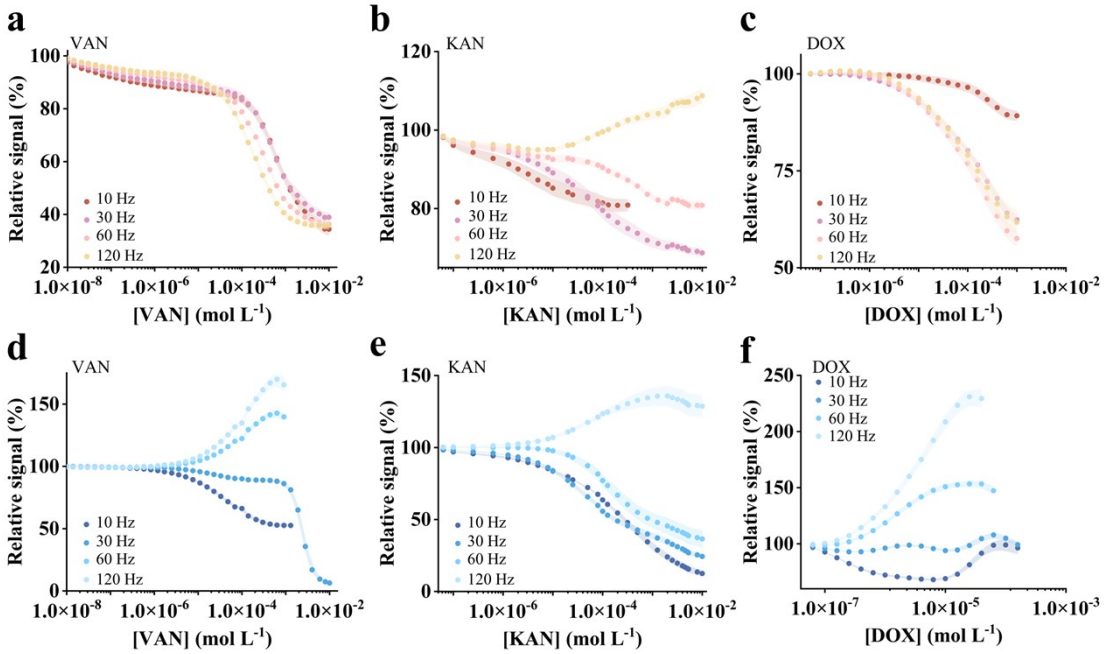

Figure S19. The titration data of varied SAMs-based EAB sensors at varied testing frequencies. We selected the optimal testing frequency for each SAM based on the stability of the baseline. VAN-C≡CH:120 Hz, VAN-SH:10 Hz. KAN-C≡CH:30 Hz, KAN-SH:30 Hz, DOX-C≡CH:120 Hz, DOX-SH:120 Hz.

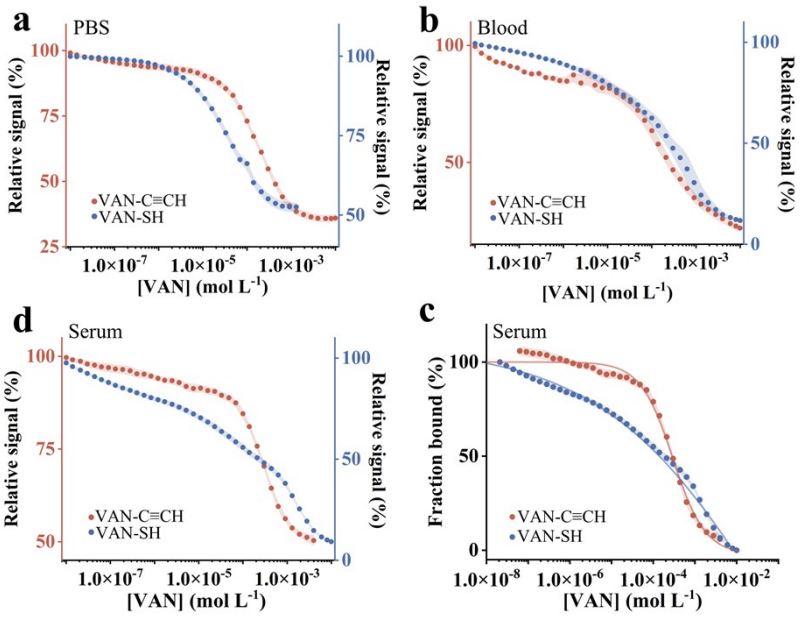

Figure S20. (a) The titration curves of vancomycin-detecting EAB sensors in PBS, (b) blood, (c) titration curves and (d) sensitivity of vancomycin-detecting EAB sensors in serum.

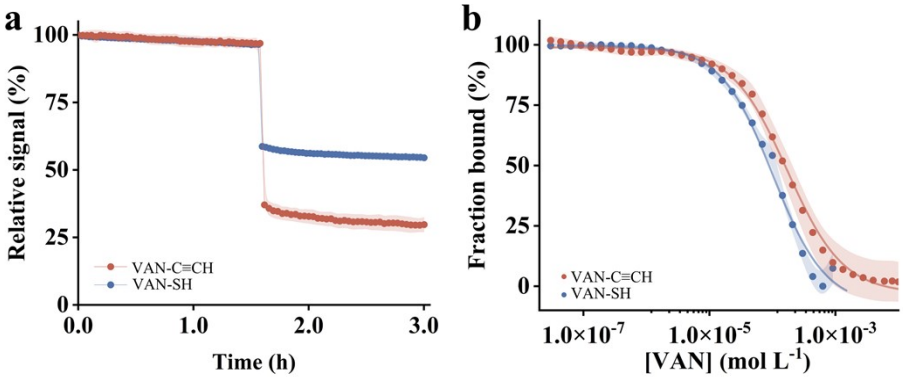

Figure S21. To maintain a consistent grafting density, the DNA concentration was adjusted to 0.05 μM, after which the (a) kinetics and (b) titration behavior of VAN-SH in PBS were investigated.

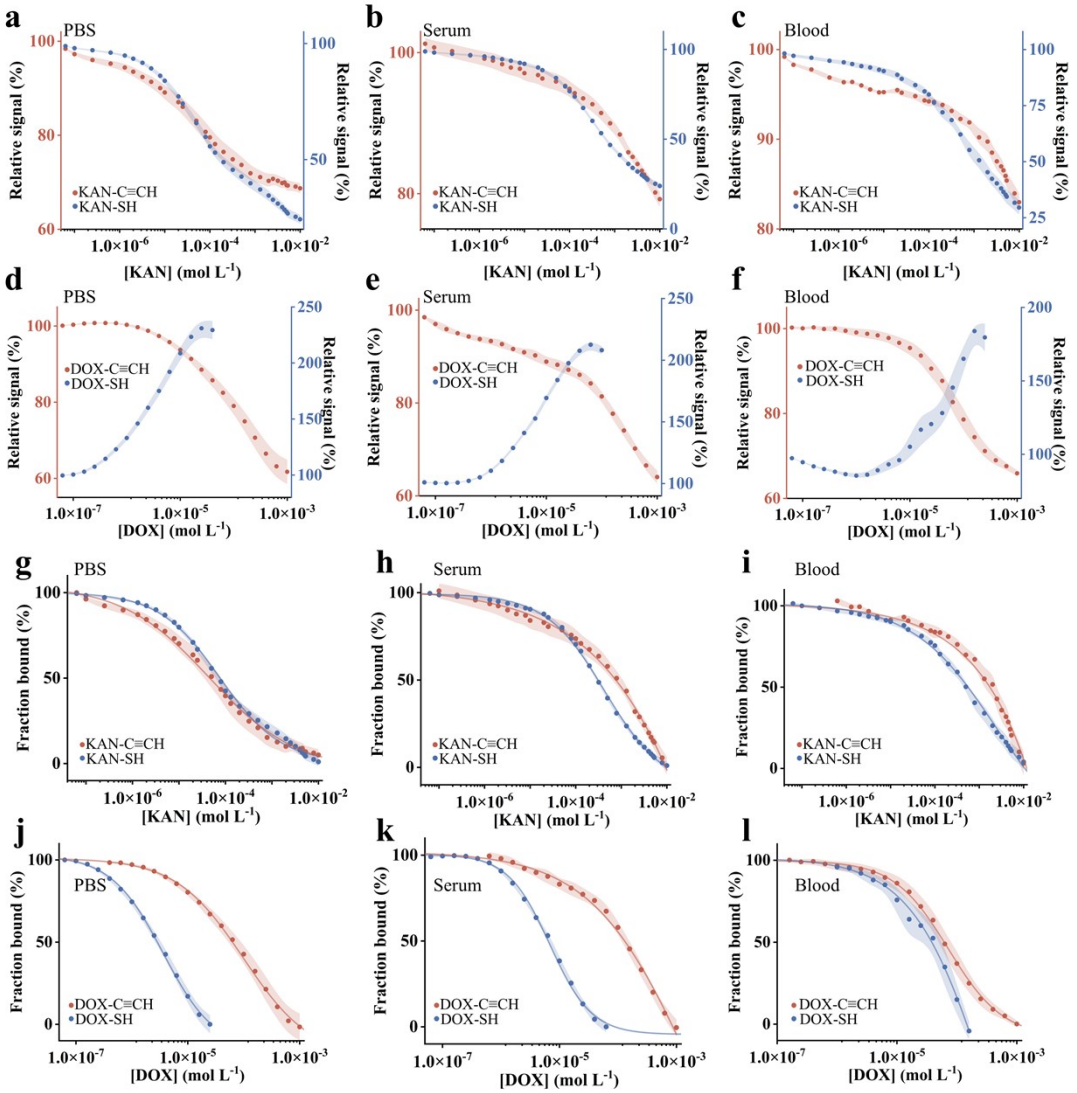

Figure S22. (a-c) The titration curves of kanamycin-detecting EAB sensors in PBS, serum and blood, respectively. (d-f) The titration data of doxorubicin-detecting EAB sensors in PBS, serum and blood, respectively. (g-i) The fraction bound curves of kanamycin-detecting EAB sensors in PBS, serum and blood, respectively. (j-l) The fraction bound curves of doxorubicin-detecting EAB sensors in PBS, serum and blood, respectively.

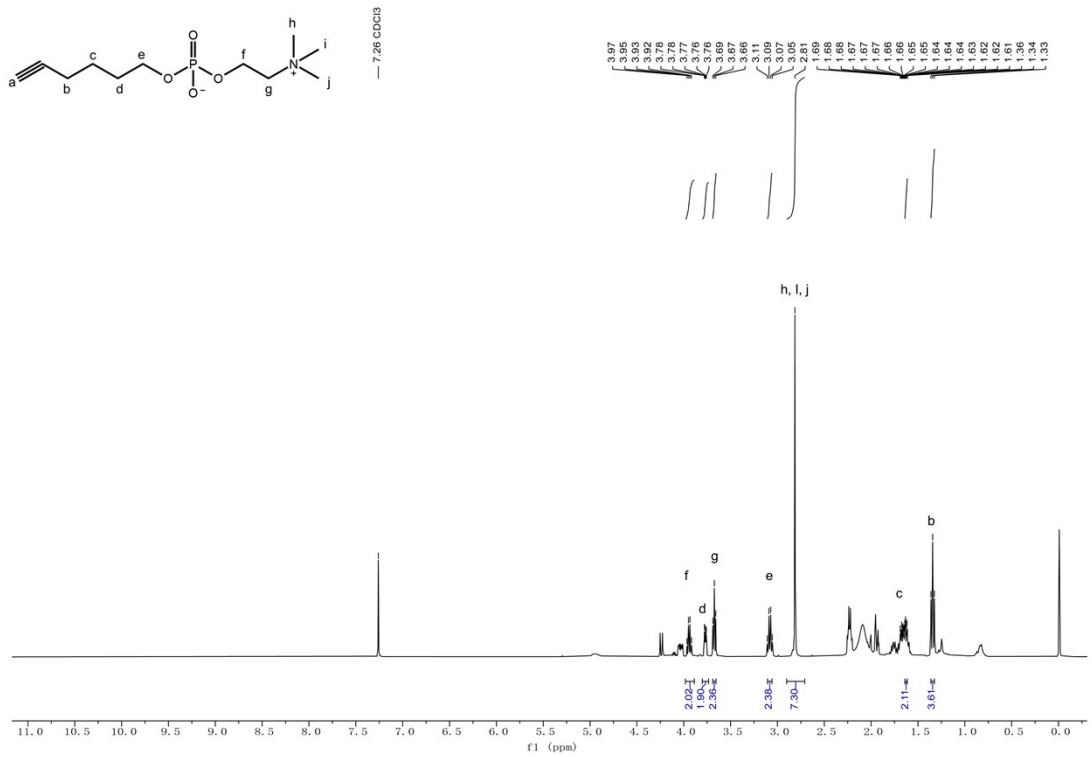

Figure S23. 1H-NMR spectrum (400 MHz, in $CDCl_3$). 3.92-3.97 (dd, 2H), 3.76-3.78 (t, 2H), 3.66-3.69 (s, 2H), 3.05-3.11 (dd, 2H), 2.81 (s, 9H), 1.61-1.64(m, 2H), δ =1.33-1.36 (t, 2H).

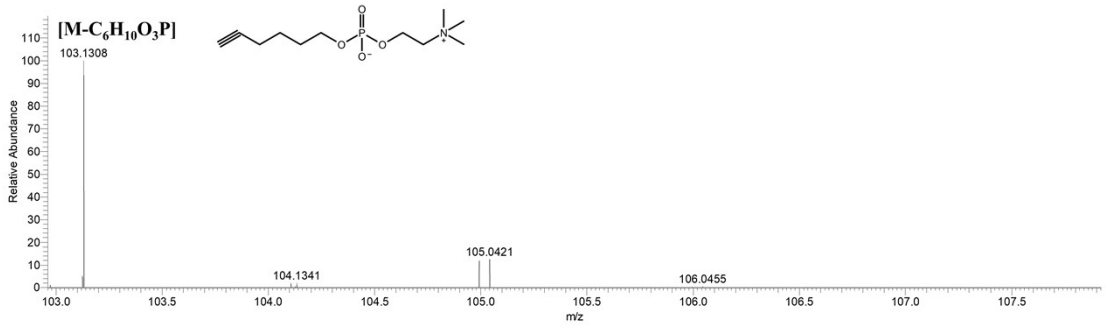

Figure S24. ESI mass spectrum of HPC. The mass of mercapto based analog compounds calculated: 103.0997 Da; observed: 103.1308 Da [M-$C_6H_{10}O_3P$].

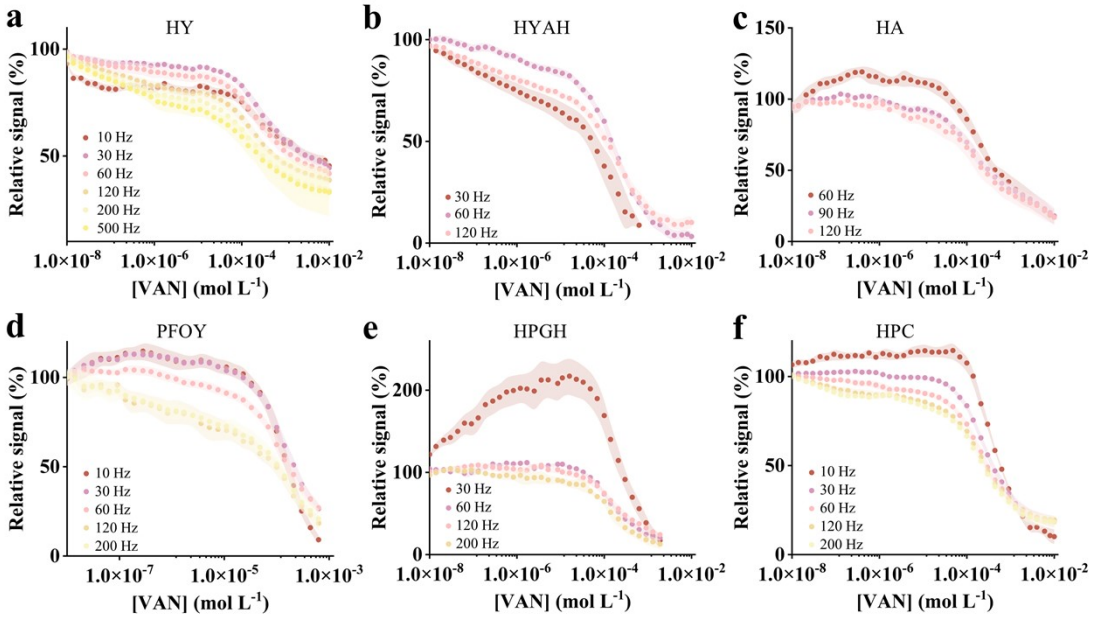

Figure S25. The optimization of interrogating frequencise of varied SAMs-based EAB sensors. We selected the optimal testing frequency for each SAM based on the stability of the baseline. Specifically, the optimal frequency for HY is 30 Hz due to the baseline at lower concentrations is flat and with a good transition upon the high concentration of target molecules. Similarly, the optimal frequency selected for HYAH was selected as 60 Hz, HA as 120Hz, PFOY as 30Hz, HPGH as 120 Hz, HPC as 30 Hz.

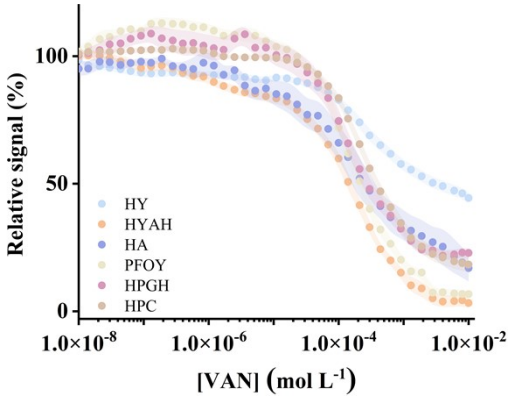

Figure S26. The titration curves of different SAMs in blood.

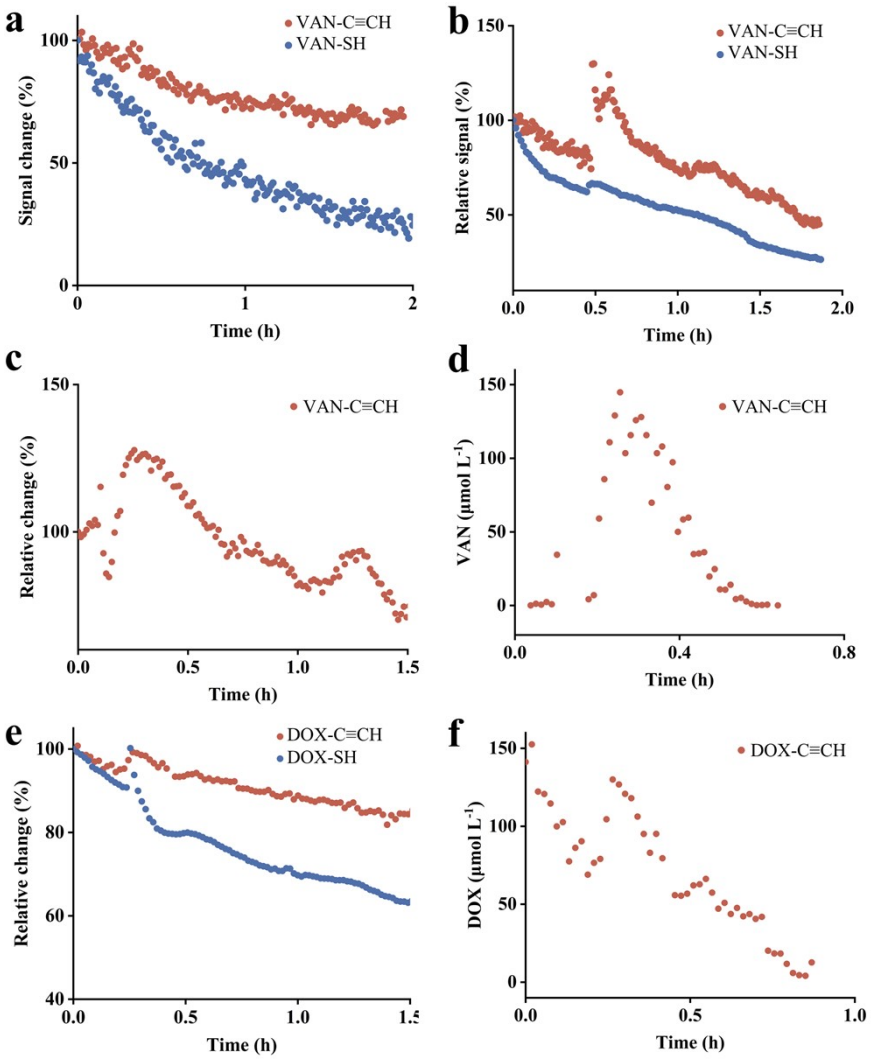

Figure S27. The replicates of in-vivo studies including both alkyne- and thiol-anchoring sensors.

Table S1. The wettability of MCH- and HYO-modified electrode surfaces, as well as that of the unmodified (bare) electrode surface; their wettability after blood exposure; antifouling performance; and surface coverage.

Characteristic \ SAMs	Bare	MCH	HYO
Wettability water (°)	97.6	67.7	73.6
Wettability blood (°)	48.4	58.1	62.9
Wettability change (°)	49.2	9.6	10.7
Area occupancy (%)	54.7	50.6	40.2
R_{ct} (Ω)	140.2	1109.2	10701.3
Surface coverage (%)	/	88.6	98.7

Table S2. Net Bader charges for HYA and MCH molecules (the negative sign "-" means gaining electrons, positive sign "+" means losing electrons).

Structure	Net Bader charges	
	Au (111)	Molecule
HYO	+0.2e	-0.2e
MCH	+0.08e	-0.08e

Table S3. A summary of the K_D values of the EAB sensors in PBS, serum and blood.

Sensor	K_D (μmol L^{-1})		
	PBS	Serum	Blood
VAN-C≡CH	162	295	197
VAN-SH	40	139	261
KAN-C≡CH	45	752	1720
KAN-SH	75	435	551
DOX-C≡CH	99	130	72
DOX-SH	4	7	38

Table S4. The wettability of electrode surfaces modified with different SAMs, their wettability after blood exposure, antifouling performance, and surface coverage.

Characteristic \ SAMs	HY	HYO	HYAH	HA	PFOY	HPGH	HPC
Wettability water (°)	80.5	73.6	74.3	65.4	91.6	89.6	66.6
Wettability blood (°)	37.9	62.9	47.2	40.1	47.4	36.4	58.1
Wettability change (°)	42.6	10.7	27.1	25.3	44.2	53.2	8.5
Area occupancy (%)	45.3	40.2	70.9	38.3	54.7	47.9	27.0
R_{ct} (Ω)	3854.0	10701.3	3046.7	10554.0	7081.0	2947.7	20872.0
Surface coverage (%)	95.0	98.7	93.6	98.4	98.5	92.2	98.9

Table S5. A summary of sensor performance including K_D, LOD, electron transfer rates and selectivity parameters of alkyne-anchoring sensors fabricated from varied SAMs.

	Blood						
	HY	HYO	HYAH	HA	PFOY	HPGH	HPC
K_D (μmol L^{-1})	416.7	196.6	154.9	182.9	169.5	166.2	275.9
LOD (μmol L^{-1})	14.8	6.0	7.3	4.4	15.0	14.2	32.4
electron transfer rate (s^{-1})	212.4	188.8	354	118	212.4	165.2	/
SFE	55.6	55.8	12.1	59.6	18.3	21.7	35.4

Table S6. The pharmacokinetic parameters of EAB sensors deployed in vivo in the living animals. C_{max} is the maximum drug concentration; T_{max} is the time at C_{max}; AUC_{all} is the area under the concentration–time curve from time zero to the last quantifiable point, indicating drug exposure over the observed period; K_{el} is the elimination rate constant of the drug; $t_{1/2}$ is the elimination half-life.

Parameter	VAN-C≡CH	DOX-C≡CH
C_{max} (μmol L^{-1})	46.33	45.61
T_{max} (h)	0.5133	0.5338
AUC_{all} (h*μmol L^{-1})	5.239	15.83
K_{el} (h^{-1})	8.712	2.549
$t_{1/2}$ (h)	0.07955	0.2719

References:

1 X. Chen, M. Li, M. Li, D. Wang, J. Zhang, Harnessing affinity-based protein profiling to reveal a novel target of nintedanib, *Chem. Comm.,* 2021, **57**, 3139-3142.

2 G. Ye, D. Wang, Y. He, X. Wang, Nunchaku-like molecules containing both an azo chromophore and a biphenylene unit as a new type of high-sensitivity photo-storage material, *J. Mater. Chem. A.,* 2010, **20**, 10680-10687.

3 N. Hada, K. Sato, J. Sakushima, Y. Goda, M. Sugita, T. Takeda, Synthetic studies on glycosphingolipids from protostomia phyla:: Synthesis of amphoteric glycolipid analogues containing a phosphocholine residue from the earthworm Pheretima hilgendorfi, *Chem. Pharm. Bull.,* 2001, **49**, 1464-1467.

4 V. Ganesh, S. K. Pal, S. Kumar, V. Lakshminarayanan, Self-assembled monolayers (SAMS) of alkoxycyanobiphenyl thiols on gold - A study of electron transfer reaction using cyclic voltammetry and electrochemical impedance spectroscopy, *J. Colloid Interface Sci. ,* 2006, **296**, 195-203.

5 L. Guan, X. Li, Q. Li, J. Guo, L. Jin, Q. Zhao, B. Liu, Relaxation and electronic states of Au(100), (110) and (111) surfaces, *Solid State Commun.,* 2009, **149**, 1561-1564.

6 C. Kittel, Introduction to solid state physics seventh, *JohnWiley and Dons. Inc., New York, NY. ,* 1996.

7 S. P. Ong, W. D. Richards, A. Jain, G. Hautier, M. Kocher, S. Cholia, D. Gunter, V. L. Chevrier, K. A. Persson, G. Ceder, Python Materials Genomics (pymatgen): A robust, open-source python library for materials analysis, *Comput. Mater. Sci.,* 2013, **68**, 314-319.

8 K. Momma, F. Izumi, VESTA 3 for three-dimensional visualization of crystal, volumetric and morphology data, *J. Appl. Crystallogr.,* 2011, **44**, 1272-1276.

9 J. P. Perdew, K. Burke, M. Ernzerhof, Generalized gradient approximation made simple, *Phys. Rev. Lett.,* 1996, **77**, 3865-3868.

10 S. Grimme, S. Ehrlich, L. Goerigk, Effect of the Damping Function in Dispersion Corrected Density Functional Theory, *J. Comput. Chem.,* 2011, **32**, 1456-1465.

11 W. Tang, E. Sanville, G. Henkelman, A grid-based Bader analysis algorithm without lattice bias, *J. Phys.: Condens. Matter.,* 2009, **21**, No. 084204.

12 E. Sanville, S. D. Kenny, R. Smith, G. Henkelman, Improved grid-based algorithm for Bader charge allocation, *J. Comput. Chem.,* 2007, **28**, 899-908.

13 G. Henkelman, A. Arnaldsson, H. Jónsson, A fast and robust algorithm for Bader decomposition of charge density, *Comput. Mater. Sci.,* 2006, **36**, 354-360.

14 M. Yu, D. R. Trinkle, Accurate and efficient algorithm for Bader charge integration, *J. Chem. Phys.,* 2011, **134**, No. 064111.